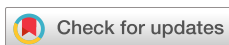


RESEARCH ARTICLE | OCTOBER 22 2021

## Near-field imaging of plasmonic nanopatch antennas with integrated semiconductor quantum dots

Vasudevan Iyer  ; Yoong Sheng Phang  ; Andrew Butler  ; Jiyang Chen; Brian Lerner  ; Christos Argyropoulos  ; Thang Hoang  ; Benjamin Lawrie  



*APL Photonics* 6, 106103 (2021)  
<https://doi.org/10.1063/5.0065524>

CHORUS



## Articles You May Be Interested In

## Fabrication of doubly resonant plasmonic nanopatch arrays on graphene

*Appl. Phys. Lett.* (June 2013)

# Engineering hyperbolicity and plasmon canalization for resonant plasmonic anisotropic nanopatch-based metasurfaces

*J. Appl. Phys.* (June 2024)

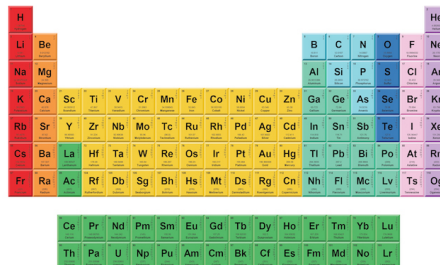
Mechanical nano-manipulation for the novel single photon sources with hybrid nanoantennas

AIP Conf. Proc. (July 2023)



THE MATERIALS SCIENCE MANUFACTURER®

# Now Invent.<sup>TM</sup>



American Elements  
Opens a World of Possibilities

*...Now Invent!*

[www.americanelements.com](http://www.americanelements.com)

# Near-field imaging of plasmonic nanopatch antennas with integrated semiconductor quantum dots

Cite as: APL Photon. 6, 106103 (2021); doi: 10.1063/5.0065524

Submitted: 2 August 2021 • Accepted: 3 October 2021 •

Published Online: 22 October 2021



Vasudevan Iyer,<sup>1</sup> Yoong Sheng Phang,<sup>2</sup> Andrew Butler,<sup>3</sup> Jiyang Chen,<sup>4</sup> Brian Lerner,<sup>5</sup> Christos Argyropoulos,<sup>3</sup> Thang Hoang,<sup>4</sup> and Benjamin Lawrie<sup>1,6,7,a)</sup>

## AFFILIATIONS

<sup>1</sup> Center for Nanophase Materials Sciences, Oak Ridge National Laboratory, Oak Ridge, Tennessee 37831, USA

<sup>2</sup> University of Georgia, Athens, Georgia 30602, USA

<sup>3</sup> Department of Electrical and Computer Engineering, University of Nebraska-Lincoln, Lincoln, Nebraska 68588, USA

<sup>4</sup> Department of Physics and Materials Science, University of Memphis, Memphis, Tennessee 38152, USA

<sup>5</sup> Department of Electrical and Computer Engineering, Duke University, Durham, North Carolina 27708, USA

<sup>6</sup> Quantum Science Center, Oak Ridge, Tennessee 37831, USA

<sup>7</sup> Materials Science and Technology Division, Oak Ridge National Laboratory, Oak Ridge, Tennessee 37831, USA

<sup>a)</sup>Author to whom correspondence should be addressed: lawriebj@ornl.gov

## ABSTRACT

Plasmonic nanopatch antennas that incorporate dielectric gaps hundreds of picometers to several nanometers thick have drawn increasing attention over the past decade because they confine electromagnetic fields to grossly sub-diffraction-limited volumes. Substantial control over the optical properties of excitons and color centers confined within these plasmonic cavities has already been demonstrated with far-field optical spectroscopies, but near-field optical spectroscopies are essential for an improved understanding of the plasmon–emitter interaction at the nanoscale. Here, we characterize the intensity and phase-resolved plasmonic response of isolated nanopatch antennas by cathodoluminescence microscopy. Furthermore, we explore the distinction between optical and electron beam spectroscopies of coupled plasmon–exciton heterostructures to identify constraints and opportunities for future nanoscale characterization and control of hybrid nanophotonic structures. While we observe substantial Purcell enhancement in time-resolved photoluminescence spectroscopies, negligible Purcell enhancement is observed in cathodoluminescence spectroscopies of hybrid nanophotonic structures. The substantial differences in measured Purcell enhancement for electron beam and laser excitation can be understood as a result of the different selection rules for these complementary experiments. These results provide a fundamentally new understanding of near-field plasmon–exciton interactions in nanopatch antennas, which is essential for myriad emerging quantum photonic devices.

© 2021 Author(s). All article content, except where otherwise noted, is licensed under a Creative Commons Attribution (CC BY) license (<http://creativecommons.org/licenses/by/4.0/>). <https://doi.org/10.1063/5.0065524>

17 July 2025 15:50:59

## I. INTRODUCTION

Plasmonic heterostructures that offer grossly sub-diffraction-limited field confinement have been a topic of intense research interest for much of the past 20 years.<sup>1–5</sup> This nanoscale field confinement has enabled advances in optical information processing,<sup>6</sup> photocatalysis,<sup>7</sup> and plasmon enhanced sensors and

spectroscopies,<sup>4,8,9</sup> as well as a variety of studies of plasmonic analog to cavity quantum electrodynamics.<sup>2,10–15</sup> While conventional lithographically patterned plasmonic nanostructures such as split ring resonators,<sup>16</sup> bowtie antennas,<sup>17</sup> nanodisks,<sup>11</sup> and other nanopatterned resonators<sup>18</sup> can offer a sufficiently small mode volume to enable the exploration of weak and strong plasmon–exciton coupling,<sup>11,12,19</sup> the emergence of gap plasmon modes that are

confined to gaps of order 1 nm has enabled substantially increased flexibility in the control of the optical properties of excitons and color centers confined within the gap.<sup>2,10,13–15</sup> Plasmonic nanogap heterostructures have been used to enhance the quantum efficiency of defect and exciton emission in the weak coupling regime,<sup>14,15,20–23</sup> to modify optical properties in the strong coupling regime,<sup>24–26</sup> and for applications ranging from gas sensing,<sup>27</sup> water splitting,<sup>28</sup> and carbon capture<sup>29</sup> to the non-invasive study of nanoparticle dynamics in liquids.<sup>30</sup> Electrical tuning of the resonance frequency of nanogap antennas has also been demonstrated as part of the move toward more functional nanophotonic devices.<sup>31</sup>

While finite difference time domain (FDTD) simulations and finite element models (FEM) are widely used to simulate the near-field optical response of plasmonic cavities, inhomogeneities in the actual devices ultimately constrain the photonic response. Conventional diffraction-limited optical microscopies are limited to spatial resolution of order 250 nm at visible wavelengths. A clear understanding of plasmonic near-field interactions with substantially better spatial resolution is essential for uncovering structure–function relationships for nanophotonic media beyond idealized numerical calculations. Super-resolution optical microscopies such as stimulated emission depletion (STED) microscopy, photoactivated localization microscopy (PALM), stochastic optical reconstruction microscopy (STORM), optical superlens imaging, and scanning near-field optical microscopy (SNOM) can be used to probe optical properties of matter with a spatial resolution of 10 to several tens of nanometers,<sup>32–35</sup> though each approach comes with some challenges. An ideal approach to super-resolution microscopy might offer true nanometer spatial resolution, access to spectrally resolved excitation and relaxation dynamics, and high-speed operation with high collection efficiency, but no such platform currently exists. Techniques such as electron energy loss spectroscopy (EELS) and cathodoluminescence (CL) microscopy are well suited to study the near-field optical properties of plasmonic heterostructures<sup>36–38</sup> and hybrid plasmon–emitter heterostructures.<sup>39</sup> CL microscopies rely on a converged electron beam to locally excite nanophotonic materials while collecting the light emitted from the material after electron beam excitation. They can provide 3 nm spatial resolution with high spectral resolution,<sup>40</sup> though their spatial resolution is generally limited by free-carrier migration and the required electron beam doses can be an obstacle for environmentally sensitive samples.

In this work, we use CL microscopy to map localized and propagating plasmon modes in the proximity of silver (Ag) nanopatch antennas (NPAs) and analyze the effect of this plasmon mode structure on CdSe/ZnS core–shell quantum dots (QDs) deposited within the NPA. We compare the results with steady state and time-resolved photoluminescence (TRPL) measurements. Furthermore, we perform FEM simulations that improve our understanding of the plasmonic modes observed in CL. Finally, we observe interference between electron beam generated transition radiation and surface plasmon polaritons (SPPs) scattered from the NPA. Notably, while substantial Purcell enhancement is observed in the time-resolved photoluminescence (TRPL) spectra, negligible Purcell enhancement is observed in the CL spectra as a result of different selection rules for electron beam and optical excitations. Combining CL microscopy of nanoplasmonic modes with PL microscopy of plasmon–exciton interactions is thus essential for understanding

plasmon–exciton interactions in nanopatch antennas that are essential for a plethora of emerging applications, such as light absorbers, photodetectors, and photon sources.

## II. SPECTRUM IMAGING OF INDIVIDUAL NANOPATCH ANTENNAS

The nanopatch heterostructures explored here comprise Ag nanocubes with 75-nm edges dropcast onto a 100-nm gold (Au) thin film. A 3–5 nm spacer layer is deposited between the Au film and the nanocube to minimize charge transfer and to maximize field confinement within the spacer layer. For initial spectroscopic mapping of the plasmon modes, a 3 nm ZnO spacer layer was deposited on the Au films on silicon substrates by atomic layer deposition. For subsequent spectroscopies of coupled plasmon–exciton heterostructures, a peel-and-stick technique was used to transfer gold films with sub-nm surface roughness onto a glass substrate, onto which a polyelectrolyte (PE) spacer layer (3 nm in thickness) was deposited using a dip-coating technique, and CdSe/ZnS core–shell QDs (Sigma-Aldrich, product number 900249) were then spin cast before Ag nanocube deposition. A cross-sectional schematic of the fabricated NPA heterostructures and a schematic representation of the CL collection optics are shown in Fig. 1.

The nanocube's plasmonic modes were probed directly by CL microscopy in a FEI Quattro environmental scanning electron

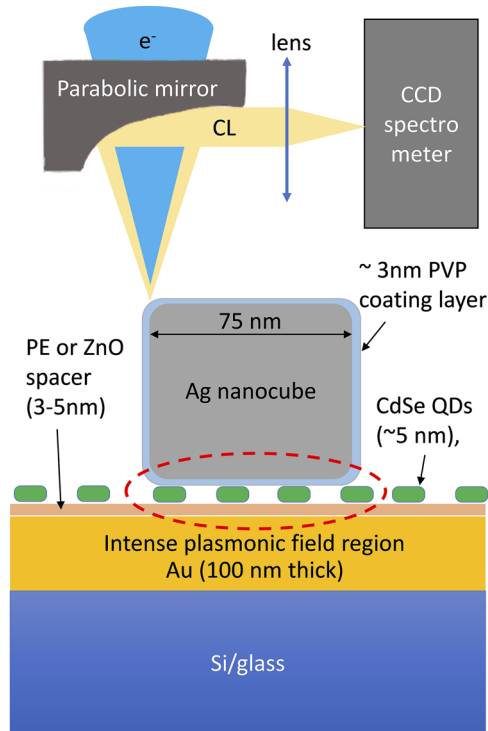


**FIG. 1.** Schematic of a nanopatch antenna heterostructure. QDs are sandwiched between the spacer layer and the nanocube. The cathodoluminescence is obtained by exciting the structure with an electron beam in an SEM and using a high NA parabolic mirror to collect light onto a spectrometer. The image is not to scale.

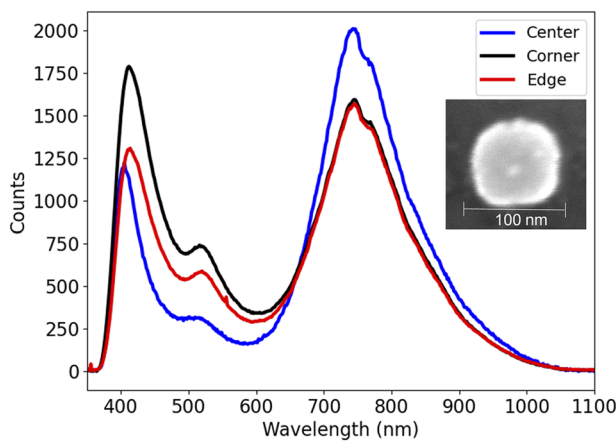


**FIG. 2.** Nanopatch antenna CL spectra for heterostructures with a polyelectrolyte spacer layer. The inset shows the SEM image of the cube. The spectra show three peaks corresponding to corner, edge, and gap plasmon modes. The three spectra were obtained with the electron beam positioned at the center, corner, and edge, respectively.

microscope (ESEM) with a Delmic Sparc CL collection system. All data described here were acquired with a beam energy of 30 keV, and beam currents of 630–5600 pA were used depending on sample robustness. While the ESEM can operate in a high vacuum or water vapor environment, all data reported here were taken in a background pressure of 40 Pa of water vapor in order to minimize charging and carbon deposition during long spectrum image acquisitions. The NPAs on the PE layer display three prominent plasmon modes centered at wavelengths of ~400, 520, and 750 nm, as shown in Fig. 2 for a typical nanocube. The inset shows the SEM image of the cube. The mode around ~750 nm is strongest when the electron beam is in the center whereas the mode around ~400 nm is strongest near the corner. The edge mode is weakly excited at the center. However, the point spectra by themselves provide only a limited understanding of the heterostructure's plasmonic response. The edge and corner modes were previously observed in the near field with EELS<sup>41</sup> for nanocube assemblies (different from the current nanopatch antenna system), but EELS cannot distinguish the radiative and non-radiative modes, a critical requirement for hybrid plasmon–exciton heterostructures.

The spectrum images shown in Fig. 3 for a NPA on a ZnO spacer layer depict the spatial distribution of distinct modes

17 July 2025 15:50:59

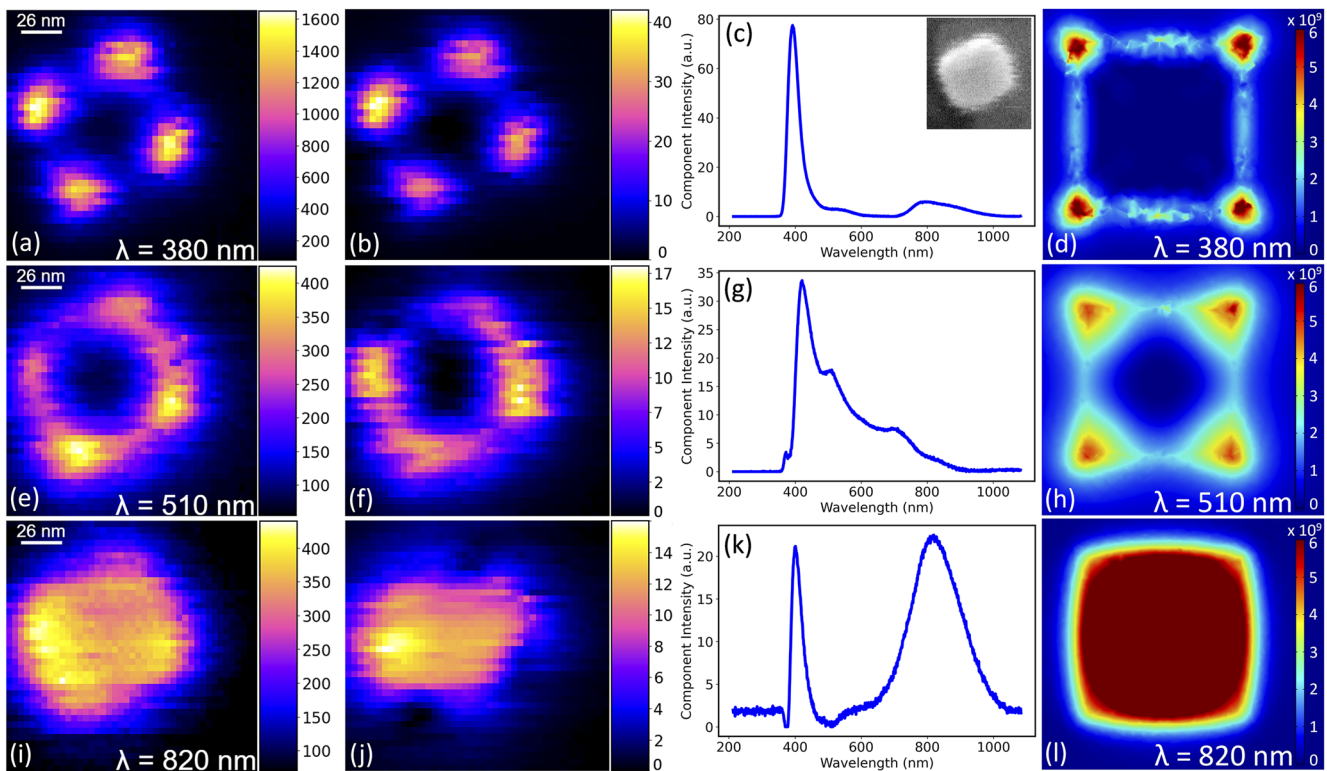


**FIG. 3.** Spectrum images of plasmon resonances supported by Ag nanocube heterostructures with a ZnO spacer layer on Au thin films. Left column (a), (e), and (i): raw measured CL intensity maps at wavelengths of 380, 510, and 820 nm (with 5 nm bandwidth for each image), second column (b), (f), and (j): the largest three of four NMF decomposition components, third column (c), (g), and (k): associated NMF spectra for each component, and right column (d), (h), and (l): FEM simulations of the electric field induced by the electron beam in the gap between the nanocube and the Au thin film at the same wavelengths used in the left column. The inset in (c) shows a SE image of the NPA acquired concurrently with the CL data reported here.

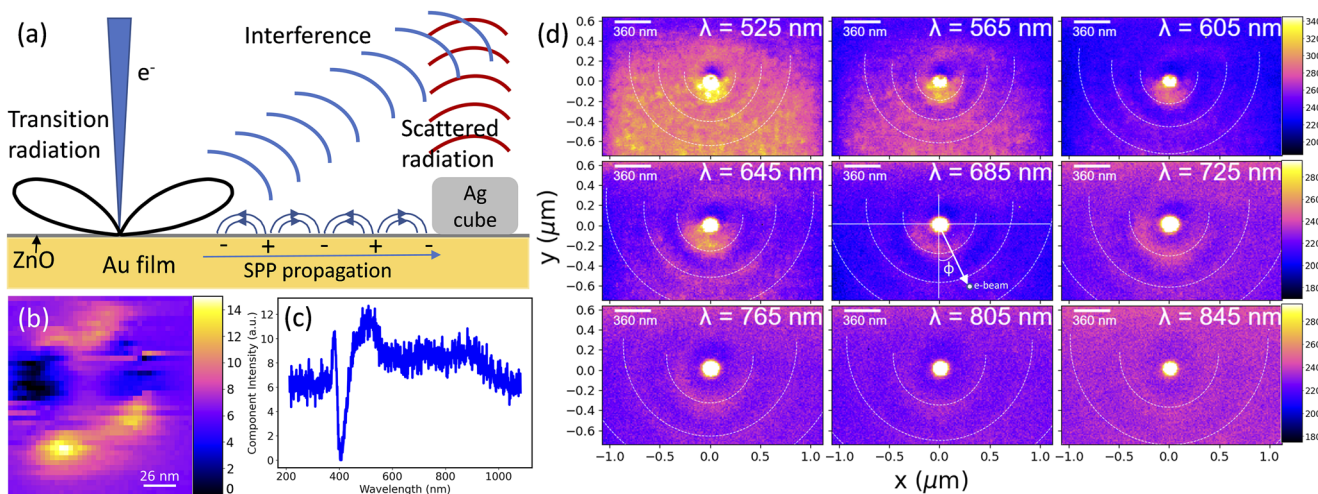


**FIG. 4.** Interference of electron beam generated transition radiation and scattered surface plasmons from the NPA. (a) Schematic of transition radiation and SPP generation at the point of electron beam incidence, followed by SPP propagation and scattering by NPA. The interference is observed in the far field. (b) and (c) Final NMF component images from the NMF decomposition shown in Fig. 3. (d) Interference patterns as the electron beam is scanned over a large area surrounding the nanocube. The colorbar is over-saturated near the NPA to enable a clearer image of the weak interference fringes.

supported by the nanocube. The images shown in the left column [Figs. 3(a), 3(e), and 3(i)] represent the raw CL intensity at wavelengths of 380, 510, and 820 nm that best represent the corner, edge, and gap plasmon modes. The gap mode is red-shifted relative to the NPA on a PE spacer layer due to the changed dielectric environment. However, simply plotting CL images associated with a limited number of wavelengths tends to obscure the information within the larger spectrum image. Hence, we used non-negative matrix factorization (NMF) to decompose the spectrum image into relevant spectral components. NMF has become a widely used tool for analysis of hyperspectral microscopies because it offers a computationally inexpensive approach to extract sparse, physically relevant data from multidimensional data.<sup>42,43</sup>

Figures 3(b), 3(f), and 3(j) show the three most prominent modes obtained by four-component NMF, which closely match the modes identified in the raw CL intensity maps (the fourth component is described in Fig. 4). The NMF spectra for each of the three components are shown in Figs. 3(c), 3(g), and 3(k). Notably, while the NMF decomposition identifies a high quality-factor corner plasmon resonance, the edge mode exhibits some additional spectral complexity and the gap plasmon mode exhibits a clear bimodal response. This may be explained in part by the fact that the NMF decomposition only assumes that each component is non-negative, but it is also suggestive of mode coupling, which is not directly evident in the intensity plots. These raw intensity plots and NMF decompositions are largely consistent with FEM simulations of the plasmonic field confinement induced by a line current source emulating an “electron beam” (as shown in the right column of Fig. 3). The nanocubes are spatially well separated (10s of  $\mu\text{m}$ ) on the substrate, and hence the simulations were performed on individual nanocubes without considering coupling between them. We expect that the differences between simulation and the experiment arise primarily due to the inhomogeneities in the nanostructure,

i.e., morphological imperfections in the nanocubes and substrate. While simulations allow us to understand the behavior of model plasmonic heterostructures, CL microscopy allows us to probe experimentally achievable, imperfect heterostructures.

### III. PLASMON INTERFERENCE WITH TRANSITION RADIATION

Nanoparticles on metallic planes can act as an antenna to couple free space photons with surface plasmon polaritons (SPPs).<sup>44</sup> It is crucial to understand this coupling for the current nanopatch antenna system to engineer nanophotonic devices that rely on the out coupling of SPPs to the far field. Notably, the final component of the NMF decomposition shown in Fig. 3 [shown in Figs. 4(b) and 4(c)] is weak compared with the localized modes, and it is very broadband except for an artifact associated with the strong corner modes near 400 nm. It is consistent with broadband SPP modes scattering at the nanocube, but this high resolution image provides no detailed understanding of the SPP propagation on the Au film. Thus, we acquired spectrum images with larger fields of view to characterize interference between transition radiation and SPP CL. This interference allows for near-field imaging of the phase of surface plasmon polaritons before they scatter off the nanocube.<sup>36,45</sup> A clear understanding of SPP propagation combined with the above imaging of nanogap plasmon modes is critical to understanding the composite plasmon-exciton interaction. This understanding is also essential for the ultimate development of dissipative-driven entanglement schemes that rely on coupling multiple emitters to shared plasmonic reservoirs.<sup>46,47</sup> Broadband transition radiation is generated when the image-charge-induced dipole in the metal is destroyed as the electron enters the metal. The electron beam also launches SPPs in the metal, which propagate outward. The SPP is scattered into free space photons when it interacts with the nanopatch antenna.<sup>48</sup>

A schematic of this process is shown in Fig. 4(a). This scattered radiation has a characteristic phase relative to the transition radiation depending on the distance of the cube from the electron beam. Therefore, the scattered beam and transition radiation can interfere to produce the interferograms shown in Fig. 4(d).

The radial distance that satisfies the interference condition is given by<sup>44</sup>

$$R = \frac{\Phi_{osc} + 2m\pi}{k_{spp} + k \sin \theta \cos \phi} + \Delta, \quad (1)$$

where  $\Phi_{osc}$  is the phase of the field scattered from the NPA,  $m$  is an integer,  $k_{spp}$  is the plasmon wave vector that is equal to  $k\sqrt{\frac{\epsilon_1\epsilon_2}{\epsilon_1+\epsilon_2}}$ , where  $\epsilon_1$  and  $\epsilon_2$  are the permittivities of ZnO and the metal film, respectively,  $\phi$  is the azimuthal angle between the NPA and the point of electron beam incidence, and  $\Delta$  is the phase arising due to the distance between the plasmon origin and the NPA. It was previously reported that the phase  $\Phi_{osc}$  is zero away from plasmon resonances,<sup>44</sup> and hence due to the high energy of the corner and edge modes (<520 nm), we set  $\Phi_{osc} = 0$  in the wavelength range of 525–825 nm, where we observed interference. The parabolic mirror collects all angles  $\theta$  from  $0^\circ$  to  $\sim 90^\circ$ , and we display the fitting result for  $\theta = 45^\circ$  as white dashed lines in Fig. 4(d). The thickness of the measured fringes is understood by changing  $\theta$  from  $0^\circ$  to  $\sim 90^\circ$ . We plot the calculated fringes for  $-110^\circ < \phi < 110^\circ$  due to the reduced experimental signal to noise at higher angles.  $\Delta$  was chosen as  $0.17\lambda_{spp}$ ,  $0.35\lambda_{spp}$ , and  $0.7\lambda_{spp}$  for the first, second, and third interference fringes for all images. Good agreement is obtained between the experimental and theoretical results. This technique can be used for any plasmonic nanoparticle shape to obtain the phase delay and scattering phase.

#### IV. COUPLED NANOPATCH QUANTUM DOT HETEROSTRUCTURES

While CL microscopy enables clear spectrum imaging of nanogap plasmon modes in these NPAs by using ZnO as the spacer layer, the PE layer was moderately deformed by the electron beam during image acquisition. This deformation did not substantially change the optical properties of the nanogap plasmon modes as evidenced by the spectra in Fig. 2, but it did modify the morphology of the substrate sufficiently to make drift compensation problematic for long acquisition-time spectrum images. As a result, spectrum images presented in Fig. 3 are for the isolated nanocubes on Au film coated silicon substrates with ZnO spacer layers. In the following text, we compare the CL emission for two different cases where QDs are deposited on a PE spacer layer (on a Au film) with or without nanocubes. The colloidal CdSe/ZnS QDs have a spherical shape and a diameter of  $\sim 5$  nm. The small diameter is necessary in order to achieve substantial field localization in the plasmon gap mode, and thus, optimize the plasmon–exciton interaction strength. We find that in contrast to the PE surface, it is a challenge to adhere the QDs directly on a ZnO surface (prior to the nanocube deposition). It is also noted that, to date, there has been no careful comparison of the PL and CL of hybrid structures designed to exhibit large Purcell effects.

Point spectra for the quantum dots dropcast on the PE spacer layer and for the hybrid NPA–QD heterostructure are shown in Fig. 5. The data are fit with five Gaussian peaks. The quantum dot

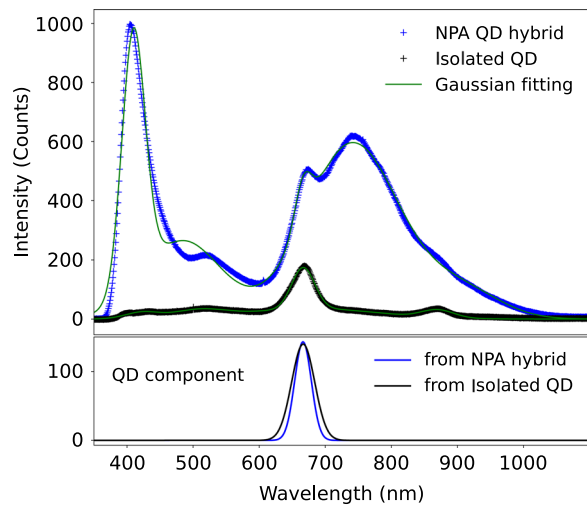


**FIG. 5.** CL emission of CdSe/ZnS QDs embedded in the NPA hybrid and on the PE layer. The spectra are fit with five Gaussian peaks, and the QD emission contribution is extracted and shown in the bottom panel for excitation on the NPA and isolated QD, respectively.

contribution to the plasmon–exciton heterostructure is extracted as one of those fit components and plotted separately in the lower panel of Fig. 5. A direct comparison is possible because the same experimental conditions are maintained by acquiring point spectra in the same area of the chip within a period of a few minutes. Compared with previous reports of quantum dot photoluminescence enhancement by nanogap plasmon modes,<sup>14</sup> the cathodoluminescence enhancement compared with the CL of isolated QDs is negligible. This is consistent with the relatively limited literature available to date exploring Purcell enhancement of exciton and defect emission by plasmonic heterostructures, where only minimal Purcell enhancement was observed.<sup>39,49,50</sup> This is not necessarily surprising because the electron beam-pumped system exhibits a very different interaction cross-section and different selection rules than the laser-pumped system.

In order to help understand the selection rules associated with electron- and laser-driven plasmon–exciton heterostructures, we acquired complementary optical dark-field (DF) scattering spectra and TRPL spectra in an optical microscope shown in Figs. 6(a) and 6(b), respectively. The DF scattering spectra of several individual NPAs shown in Fig. 6(a) exhibit a small variation in the peak wavelength, which is consistent with small variation in the nanocube size or gap thickness. Nevertheless, the NPAs' peak resonances show an excellent spectral overlap with the QD emission at around 650 nm. Notably, the measured DF scattering under optical excitation exhibits much simpler mode structure than the measured cathodoluminescence because the near-field electron beam excitation is capable of exciting optically forbidden transitions. Figure 6(b) compares the TRPL of QDs on a glass slide and in an NPA. Similar to the previously observed Purcell enhancement effect in the NPA platform, the decay time of QDs in the NPA is significantly reduced as compared to the intrinsic decay of the same QDs on a glass slide.<sup>13,14,22,51</sup> The decay of QDs on a glass slide is well fitted with a single exponential component with a lifetime of 9.5 ns. When

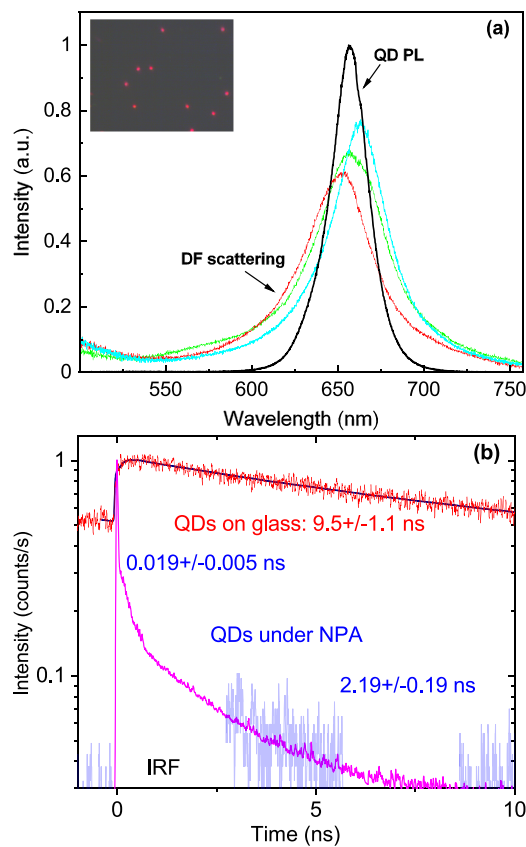


**FIG. 6.** (a) Quantum dot PL spectrum (black curve) and dark-field scattering spectra of randomly selected nanopatch antennas (colored curves). The inset displays a dark-field camera image of the NPAs under white light illumination. Individual NPAs were well separated and easily distinguished for optical spectroscopies. (b) Time-resolved PL of quantum dot emission. The red and blue curves correspond to the PL from quantum dots on glass and within the NPA, respectively. The black curve shows the instrument response function. The Purcell enhancement of the QD PL can be calculated from the fitted PL lifetimes.

the QDs are coupled to the NPA, the decay curve is fitted with a biexponential function deconvolved with the instrument response, resulting in a fast decay component of 0.019 ns and a slower component of 2.19 ns. The fast component is attributed to the decay time of the QDs that are well coupled to the NPA and the slower component is originated from QDs on the Au film, away from the nanocube but within the laser excitation spot. The reduction in the decay of the QDs on a Au film is a result of the nonradiative quenching effect. Furthermore, because the QDs are spherically symmetric, the emitted photons are randomly polarized. Because the gap mode of the NPA is vertically polarized, only photons that have a vertically polarized component can efficiently couple to the NPA resonance and contribute to the fast decay channel. As has been shown previously that the decrease in the lifetime of the QDs in the NPA is accompanied by a simultaneous increase in the PL intensity,<sup>13,14,22,51</sup> the ratio  $\tau_{\text{glass}}/\tau_{\text{NPA}} \sim 500$  represents the Purcell enhancement factor.

## V. CONCLUSION

The TRPL measurements suggest that the heterostructure is well designed with measured Purcell enhancement consistent with the literature, and the samples were transferred in vacuum from the TRPL measurement to the CL measurement, so minimal environmental degradation is expected between measurements. Therefore, the negligible measured Purcell enhancement with electron beam excitation indicates a more fundamental difference between the two measurement modalities. The near-field electron beam excitation of the NPA excites additional modes compared to those excited optically, resulting in a broader red-shifted composite NPA response, as shown in Fig. 5. Although the QD emission lies within the broadband envelope, the electron beam excitation of modes that are far from resonant with the QD results in substantially reduced plasmon-exciton interactions in the composite system.

However, while it seems clear that CL characterization of hybrid plasmon-exciton heterostructures may not yield the same Purcell enhancement measured in PL spectroscopies, CL microscopy is an indispensable tool for mapping localized and propagating plasmonic modes of technologically relevant nanopatch antenna structures with few nanometer spatial resolution. Furthermore, techniques such as electron beam induced deposition can be used to pattern plasmonic heterostructures in the SEM<sup>52,53</sup> near individual defects or excitons after imaging with CL microscopy and exert *in situ* control over plasmon-exciton interactions subject to the understanding that the composite system response will be different under laser excitation than electron beam excitation. Indeed, pump-probe spectroscopies that combine laser and electron beam excitation of the sample should allow for completely integrated experiments that probe the near-field properties of the hybrid heterostructure with an electron beam excitation while probing the resonantly excited state with a laser excitation. Ultimately, this level of integrated manipulation and characterization of hybrid nanophotonic systems is critical to the development of various recently proposed dissipative-driven entanglement schemes.<sup>46,47</sup>

## VI. METHODS

### A. CL microscopy

CL microscopy was performed in a FEI Quattro environmental scanning electron microscope with a Delmic Sparc cathodoluminescence collection system. A beam energy of 30 keV and beam currents of 630–5600 pA were used, depending on sample robustness. The sample chamber was maintained at a pressure of 40 Pa water vapor. CL spectra were collected using a parabolic mirror with a high numerical aperture of 0.9 and sent to a spectrometer (Andor Kymera 193i) equipped with a 150 line/mm grating and an Andor Newton CCD camera. Spectra were acquired using dwell times of 0.2–2 s/pixel, and spectrum images were acquired by scanning the electron beam while acquiring a CL spectrum at each pixel. Reference images were taken every 2–20 s as necessary during the spectrum image acquisition to allow for drift correction.

### B. Optical characterization

Optical responses of NPA samples were characterized by dark-field scattering and PL measurements through a customized Nikon LV 150N microscope with a 3D nanometer-resolution translation

stage (Newport, model 9063). The modified microscope has a halogen lamp for white light illumination and a modified optical path for laser excitation (Coherent laser at 475-nm, 80 MHz, 150 fs) and PL collection through a bright/dark field 100 $\times$  microscope objective lens. The dark-field scattering or PL signal from individual NPAs was filtered by a pinhole at a focal imaging plane before entering the spectrometer (Horiba iHR550) and CCD camera (Horiba Jobin-Yvon Synapse). A set of appropriate short-pass (for laser excitation) and long-pass (for PL detection) spectral filters were used for the QD excitation and PL collection. For the decay time measurements of the QDs, a time-correlated single photon counting setup was used. The PL emission from the QDs was collected by the objective lens and sent through the spectrometer for either spectral analysis or through a side exit to be guided into a fast-timing avalanche photodiode for temporal analysis. The signal collected by the photodiode was analyzed by a single photon counting module (PicoHarp 300). Final lifetimes were obtained from fits to the data deconvolved with the instrument response function by using the EasyTau software (PicoQuant).

### C. FEM simulation

Three-dimensional (3D) FEM simulations of the silver (Ag) plasmonic nanopatch antenna structures were performed using Comsol Multiphysics®. The dimensions of the nanocube were identical to the experiments and a spacer layer with a thickness of 5 nm was used. The model was surrounded with a spherical scattering boundary condition that prevented backscattering of the electromagnetic waves from the simulation boundaries. A line current was placed vertically 10 nm above the center of the nanocube to simulate the electron beam.<sup>54,55</sup> The induced field plots shown in Fig. 3 were obtained by running the simulation twice, once with the line current in vacuum and once with the line current in the presence of the nanopatch antenna, each time using the same mesh. The induced fields were obtained by using the formula  $E_{ind} = E_{ant} - E_{vac}$ , where  $E_{ant}$  is the field calculated with the nanopatch antenna structure and  $E_{vac}$  is the field calculated in vacuum. All employed materials were simulated using realistic refractive index data.<sup>56,57</sup>

### ACKNOWLEDGMENTS

This research study was carried out at the Center for Nanophase Materials Sciences (CNMS), which is sponsored at ORNL by the Scientific User Facilities Division, Office of Basic Energy Sciences, U.S. Department of Energy. Support at ORNL for hybrid quantum photonic systems was provided by the U.S. Department of Energy, Office of Science, National Quantum Information Science Research Centers, Quantum Science Center. C.A. acknowledges support from the Office of Naval Research Young Investigator Program (ONR-YIP) under Grant No. N00014-19-1-2384. T.H. acknowledges support from the National Science Foundation (NSF) (Grant No. DMR-1709612). This article has been authored by UT-Battelle, LLC, under Contract No. DE-AC05-00OR22725 with the U.S. Department of Energy (DOE). The U.S. government retains and the publisher, by accepting the article for publication, acknowledges that the U.S. government retains a nonexclusive, paid-up, irrevocable, worldwide license to publish or reproduce the published form of this

manuscript, or allow others to do so for U.S. government purposes. DOE will provide public access to these results of federally sponsored research in accordance with the DOE Public Access Plan (<http://energy.gov/downloads/doe-public-access-plan>).

### AUTHOR DECLARATIONS

#### Conflict of Interest

The authors have no conflicts to disclose.

### DATA AVAILABILITY

The data that support the findings of this study are available from the corresponding author upon reasonable request.

### REFERENCES

- <sup>1</sup>T. Wu, W. Yan, and P. Lalanne, “Bright plasmons with cubic nanometer mode volumes through mode hybridization,” *ACS Photonics* **8**, 307–314 (2021).
- <sup>2</sup>J. J. Baumberg, J. Aizpurua, M. H. Mikkelsen, and D. R. Smith, “Extreme nanophotonics from ultrathin metallic gaps,” *Nat. Mater.* **18**, 668–678 (2019).
- <sup>3</sup>S. A. Maier, P. G. Kik, H. A. Atwater, S. Meltzer, E. Harel, B. E. Koel, and A. A. G. Requicha, “Local detection of electromagnetic energy transport below the diffraction limit in metal nanoparticle plasmon waveguides,” *Nat. Mater.* **2**, 229–232 (2003).
- <sup>4</sup>S. A. Maier, “Plasmonic field enhancement and SERS in the effective mode volume picture,” *Opt. Express* **14**, 1957–1964 (2006).
- <sup>5</sup>M. L. Brongersma, J. W. Hartman, and H. A. Atwater, “Electromagnetic energy transfer and switching in nanoparticle chain arrays below the diffraction limit,” *Phys. Rev. B* **62**, R16356 (2000).
- <sup>6</sup>P. Zijlstra, J. W. M. Chon, and M. Gu, “Five-dimensional optical recording mediated by surface plasmons in gold nanorods,” *Nature* **459**, 410–413 (2009).
- <sup>7</sup>S. Linic, P. Christopher, and D. B. Ingram, “Plasmonic-metal nanostructures for efficient conversion of solar to chemical energy,” *Nat. Mater.* **10**, 911–921 (2011).
- <sup>8</sup>S. Nie and S. R. Emory, “Probing single molecules and single nanoparticles by surface-enhanced Raman scattering,” *Science* **275**, 1102–1106 (1997).
- <sup>9</sup>C. Lee, B. Lawrie, R. Pooser, K.-G. Lee, C. Rockstuhl, and M. Tame, “Quantum plasmonic sensors,” *Chem. Rev.* **121**, 4743–4804 (2021).
- <sup>10</sup>F. Benz, M. K. Schmidt, A. Dreismann, R. Chikkaraddy, Y. Zhang, A. Demetriadou, C. Carnegie, H. Ohadi, B. de Nijs, R. Esteban, J. Aizpurua, and J. J. Baumberg, “Single-molecule optomechanics in ‘picocavities’,” *Science* **354**, 726–729 (2016).
- <sup>11</sup>B. J. Lawrie, K.-W. Kim, D. P. Norton, and R. F. Haglund, Jr., “Plasmon–exciton hybridization in ZnO quantum-well Al nanodisc heterostructures,” *Nano Lett.* **12**, 6152–6157 (2012).
- <sup>12</sup>N. T. Fofang, T.-H. Park, O. Neumann, N. A. Mirin, P. Nordlander, and N. J. Halas, “Plexcitonic nanoparticles: Plasmon–exciton coupling in nanoshell–J-aggregate complexes,” *Nano Lett.* **8**, 3481–3487 (2008).
- <sup>13</sup>G. M. Akselrod, C. Argyropoulos, T. B. Hoang, C. Ciraci, C. Fang, J. Huang, D. R. Smith, and M. H. Mikkelsen, “Probing the mechanisms of large Purcell enhancement in plasmonic nanoantennas,” *Nat. Photonics* **8**, 835–840 (2014).
- <sup>14</sup>G. M. Akselrod, M. C. Weidman, Y. Li, C. Argyropoulos, W. A. Tisdale, and M. H. Mikkelsen, “Efficient nanosecond photoluminescence from infrared PbS quantum dots coupled to plasmonic nanoantennas,” *ACS Photonics* **3**, 1741–1746 (2016).
- <sup>15</sup>J. Huang, G. M. Akselrod, T. Ming, J. Kong, and M. H. Mikkelsen, “Tailored emission spectrum of 2D semiconductors using plasmonic nanocavities,” *ACS Photonics* **5**, 552–558 (2018).

- <sup>16</sup>E. Cubukcu, S. Zhang, Y.-S. Park, G. Bartal, and X. Zhang, "Split ring resonator sensors for infrared detection of single molecular monolayers," *Appl. Phys. Lett.* **95**, 043113 (2009).
- <sup>17</sup>E. X. Jin and X. Xu, "Plasmonic effects in near-field optical transmission enhancement through a single bowtie-shaped aperture," *Appl. Phys. B* **84**, 3–9 (2006).
- <sup>18</sup>R. B. Davidson, A. Yanchenko, J. I. Ziegler, S. M. Avanesyan, B. J. Lawrie, and R. F. Haglund, Jr., "Ultrafast plasmonic control of second harmonic generation," *ACS Photonics* **3**, 1477–1481 (2016).
- <sup>19</sup>R. Pamu, B. J. Lawrie, B. Khomami, and D. Mukherjee, "Broadband plasmonic photocurrent enhancement from photosystem I assembled with tailored arrays of Au and Ag nanodisks," *ACS Appl. Nano Mater.* **4**, 1209–1219 (2021).
- <sup>20</sup>T.-T. Jiang, W.-J. Shao, N.-Q. Yin, L. Liu, J.-L.-Q. Song, L.-X. Zhu, and X.-L. Xu, "Enhanced photoluminescence of CdSe quantum dots by the coupling of Ag nanocube and Ag film," *Chin. Phys. B* **23**, 086102 (2014).
- <sup>21</sup>T. B. Hoang, G. M. Akselrod, and M. H. Mikkelsen, "Ultrafast room-temperature single photon emission from quantum dots coupled to plasmonic nanocavities," *Nano Lett.* **16**, 270–275 (2016).
- <sup>22</sup>S. I. Bogdanov, M. Y. Shalaginov, A. S. Lagutchev, C.-C. Chiang, D. Shah, A. S. Baburin, I. A. Ryzhikov, I. A. Rodionov, A. V. Kildishev, A. Boltasseva, and V. M. Shalaev, "Ultrabright room-temperature sub-nanosecond emission from single nitrogen-vacancy centers coupled to nanopatch antennas," *Nano Lett.* **18**, 4837–4844 (2018).
- <sup>23</sup>Y. Luo, G. D. Shepard, J. V. Ardelean, D. A. Rhodes, B. Kim, K. Barmak, J. C. Hone, and S. Strauf, "Deterministic coupling of site-controlled quantum emitters in monolayer WSe<sub>2</sub> to plasmonic nanocavities," *Nat. Nanotechnol.* **13**, 1137–1142 (2018).
- <sup>24</sup>M.-E. Kleemann, R. Chikkaraddy, E. M. Alexeev, D. Kos, C. Carnegie, W. Deacon, A. C. de Pury, C. Große, B. de Nijs, J. Mertens, A. I. Tartakovskii, and J. J. Baumberg, "Strong-coupling of WSe<sub>2</sub> in ultra-compact plasmonic nanocavities at room temperature," *Nat. Commun.* **8**, 1296 (2017).
- <sup>25</sup>R. Chikkaraddy, B. De Nijs, F. Benz, S. J. Barrow, O. A. Scherman, E. Rosta, A. Demetriadou, P. Fox, O. Hess, and J. J. Baumberg, "Single-molecule strong coupling at room temperature in plasmonic nanocavities," *Nature* **535**, 127–130 (2016).
- <sup>26</sup>J. Qin, Y. H. Chen, Z. Zhang, Y. Zhang, R. J. Blaikie, B. Ding, and M. Qiu, "Revealing strong plasmon-exciton coupling between nanogap resonators and two-dimensional semiconductors at ambient conditions," *Phys. Rev. Lett.* **124**, 063902 (2020).
- <sup>27</sup>A. W. Powell, D. M. Coles, R. A. Taylor, A. A. R. Watt, H. E. Assender, and J. M. Smith, "Plasmonic gas sensing using nanocube patch antennas," *Adv. Opt. Mater.* **4**, 634–642 (2016).
- <sup>28</sup>D. Xu, S. Yang, Y. Jin, M. Chen, W. Fan, B. Luo, and W. Shi, "Ag-decorated ATaO<sub>3</sub> (A = K, Na) nanocube plasmonic photocatalysts with enhanced photocatalytic water-splitting properties," *Langmuir* **31**, 9694–9699 (2015).
- <sup>29</sup>W. Lu, Y. Zhang, J. Zhang, and P. Xu, "Reduction of gas CO<sub>2</sub> to CO with high selectivity by Ag nanocube-based membrane cathodes in a photoelectrochemical system," *Ind. Eng. Chem. Res.* **59**, 5536–5545 (2020).
- <sup>30</sup>C. G. Bischak, R. B. Wai, C. Cherqui, J. A. Busche, S. C. Quillin, C. L. Hetherington, Z. Wang, C. D. Aiello, D. G. Schlom, S. Aloni, D. F. Ogletree, D. J. Masiello, and N. S. Ginsberg, "Noninvasive cathodoluminescence-activated nanoimaging of dynamic processes in liquids," *ACS Nano* **11**, 10583–10590 (2017).
- <sup>31</sup>T. B. Hoang and M. H. Mikkelsen, "Broad electrical tuning of plasmonic nanoantennas at visible frequencies," *Appl. Phys. Lett.* **108**, 183107 (2016).
- <sup>32</sup>B. O. Leung and K. C. Chou, "Review of super-resolution fluorescence microscopy for biology," *Appl. Spectrosc.* **65**, 967–980 (2011).
- <sup>33</sup>D. W. Pohl, "Scanning near-field optical microscopy (SNOM)," in *Advances in Optical and Electron Microscopy* (Elsevier, 1991), Vol. 12, pp. 243–312.
- <sup>34</sup>N. Fang, H. Lee, C. Sun, and X. Zhang, "Sub-diffraction-limited optical imaging with a silver superlens," *Science* **308**, 534–537 (2005).
- <sup>35</sup>P. K. Venuthurumilli, X. Wen, V. Iyer, Y. P. Chen, and X. Xu, "Near-field imaging of surface plasmons from the bulk and surface state of topological insulator Bi<sub>2</sub>Te<sub>2</sub>Se," *ACS Photonics* **6**, 2492–2498 (2019).
- <sup>36</sup>J. A. Hachtel, S.-Y. Cho, R. B. Davidson, M. A. Feldman, M. F. Chisholm, R. F. Haglund, J. C. Idrobo, S. T. Pantelides, and B. J. Lawrie, "Spatially and spectrally resolved orbital angular momentum interactions in plasmonic vortex generators," *Light: Sci. Appl.* **8**, 33 (2019).
- <sup>37</sup>G. Pakeltis, E. Rotunno, S. Khorassani, D. A. Garfinkel, R. Collette, C. A. West, S. T. Retterer, J. C. Idrobo, D. J. Masiello, and P. D. Rack, "High spatial and energy resolution electron energy loss spectroscopy of the magnetic and electric excitations in plasmonic nanorod oligomers," *Opt. Express* **29**, 4661–4671 (2021).
- <sup>38</sup>J. A. Hachtel, R. B. Davidson, E. R. Kovalik, S. T. Retterer, A. R. Lupini, R. F. Haglund, B. J. Lawrie, and S. T. Pantelides, "Polarization- and wavelength-resolved near-field imaging of complex plasmonic modes in Archimedean nanospirals," *Opt. Lett.* **43**, 927–930 (2018).
- <sup>39</sup>M. A. Feldman, E. F. Dumitrescu, D. Bridges, M. F. Chisholm, R. B. Davidson, P. G. Evans, J. A. Hachtel, A. Hu, R. C. Pooser, R. F. Haglund, and B. J. Lawrie, "Colossal photon bunching in quasiparticle-mediated nanodiamond cathodoluminescence," *Phys. Rev. B* **97**, 081404 (2018).
- <sup>40</sup>J. Scheffold, S. Meuret, N. Schilder, T. Coenen, H. Agrawal, E. C. Garnett, and A. Polman, "Spatial resolution of coherent cathodoluminescence super-resolution microscopy," *ACS Photonics* **6**, 1067–1072 (2019).
- <sup>41</sup>B. Goris, G. Guzzinati, C. Fernández-López, J. Pérez-Juste, L. M. Liz-Marzán, A. Trügler, U. Hohenester, J. Verbeeck, S. Bals, and G. Van Tendeloo, "Plasmon mapping in Au@Ag nanocube assemblies," *J. Phys. Chem. C* **118**, 15356–15362 (2014).
- <sup>42</sup>A. Konečná, J. Li, J. H. Edgar, F. de Abajo, and J. A. Hachtel, "Revealing nanoscale confinement effects on hyperbolic phonon polaritons with an electron beam," *Small* **17**, 2103404 (2021); arXiv:2104.01997.
- <sup>43</sup>X.-Y. Liu, S. Guo, A. Ramoji, T. Bocklitz, P. Rösch, J. Popp, and H.-Q. Yu, "Spatiotemporal organization of biofilm matrix revealed by confocal Raman mapping integrated with non-negative matrix factorization analysis," *Anal. Chem.* **92**, 707–715 (2019).
- <sup>44</sup>T. Sannomiya, A. Konečná, T. Matsukata, Z. Thollar, T. Okamoto, F. J. García de Abajo, and N. Yamamoto, "Cathodoluminescence phase extraction of the coupling between nanoparticles and surface plasmon polaritons," *Nano Lett.* **20**, 592–598 (2020).
- <sup>45</sup>M. Kuttge, E. J. R. Vesseur, A. F. Koenderink, H. J. Lezec, H. A. Atwater, F. J. García de Abajo, and A. Polman, "Local density of states, spectrum, and far-field interference of surface plasmon polaritons probed by cathodoluminescence," *Phys. Rev. B* **79**, 113405 (2009).
- <sup>46</sup>E. Dumitrescu and B. Lawrie, "Antibunching dynamics of plasmonically mediated entanglement generation," *Phys. Rev. A* **96**, 053826 (2017).
- <sup>47</sup>Y. Li, A. Nemilentsau, and C. Argyropoulos, "Resonance energy transfer and quantum entanglement mediated by epsilon-near-zero and other plasmonic waveguide systems," *Nanoscale* **11**, 14635–14647 (2019).
- <sup>48</sup>A. V. Zayats, I. I. Smolyaninov, and A. A. Maradudin, "Nano-optics of surface plasmon polaritons," *Phys. Rep.* **408**, 131–314 (2005).
- <sup>49</sup>M. Jiang, L. Zheng, Y. Li, H. Shan, C. Chi, Z. Liu, Y. Huang, Z. Dang, F. Lin, and Z. Fang, "Tailoring ZnO spontaneous emission with plasmonic radiative local density of states using cathodoluminescence microscopy," *J. Phys. Chem. C* **124**, 13886–13893 (2020).
- <sup>50</sup>S. Yanagimoto, N. Yamamoto, T. Sannomiya, and K. Akiba, "Purcell effect of nitrogen-vacancy centers in nanodiamond coupled to propagating and localized surface plasmons revealed by photon-correlation cathodoluminescence," *Phys. Rev. B* **103**, 205418 (2020); arXiv:2012.11224.
- <sup>51</sup>T. B. Hoang, G. M. Akselrod, C. Argyropoulos, J. Huang, D. R. Smith, and M. H. Mikkelsen, "Ultrafast spontaneous emission source using plasmonic nanoantennas," *Nat. Commun.* **6**, 7788 (2015).
- <sup>52</sup>R. Winkler, F.-P. Schmidt, U. Haselmann, J. D. Fowlkes, B. B. Lewis, G. Kotheleitner, P. D. Rack, and H. Plank, "Direct-write 3D nanoprinting of plasmonic structures," *ACS Appl. Mater. Interfaces* **9**, 8233–8240 (2017).
- <sup>53</sup>V. Iyer, S. T. Retterer, J. Fowlkes, S. Jesse, A. A. Puretzky, J. A. Hachtel, P. D. Rack, and B. J. Lawrie, "In situ electron-beam processing and

cathodoluminescence microscopy for quantum nanophotonics,” *Proc. SPIE* **11675**, 1167504 (2021).

<sup>54</sup>P. Sutter, L. K. Khorashad, C. Argyropoulos, and E. Sutter, “Cathodoluminescence of ultrathin twisted Ge<sub>1-x</sub>Sn<sub>x</sub>S van der Waals nanoribbon waveguides,” *Adv. Mater.* **33**, 2006649 (2021).

<sup>55</sup>P. Sutter, J. S. French, L. Khosravi Khorashad, C. Argyropoulos, and E. Sutter, “Optoelectronics and nanophotonics of vapor–liquid–solid

grown GaSe van der Waals nanoribbons,” *Nano Lett.* **21**, 4335–4342 (2021).

<sup>56</sup>C. Stelling, C. R. Singh, M. Karg, T. A. F. König, M. Thelakkat, and M. Retsch, “Plasmonic nanomeshes: Their ambivalent role as transparent electrodes in organic solar cells,” *Sci. Rep.* **7**, 42530 (2017).

<sup>57</sup>P. B. Johnson and R. W. Christy, “Optical constants of the noble metals,” *Phys. Rev. B* **6**, 4370–4379 (1972).